

The problematically short superwind of OH/IR stars

Probing the outflow with the 69 μm spectral band of forsterite

B.L. de Vries¹, J.A.D.L. Blommaert^{1,2}, L.B.F.M. Waters^{3,4}, C. Waelkens¹, M. Min⁴, R. Lombaert¹, and H. Van Winckel¹

¹ Instituut voor Sterrenkunde, K.U. Leuven, Celestijnenlaan 200D, 3001 Leuven, Belgium

² Department of Physics and Astrophysics, Vrije Universiteit Brussel, Pleinlaan 2, 1050 Brussels, Belgium

³ SRON Netherlands Institute for Space Research, P.O. Box 800, 9700 AV Groningen, The Netherlands

⁴ Sterrenkundig Instituut Anton Pannekoek, University of Amsterdam, Science Park 904, 1098 XH, Amsterdam, The Netherlands

Received 27/08/2013; accepted 31/10/2013

ABSTRACT

Aims. Spectra of OH/IR stars show prominent spectral bands of crystalline olivine ($\text{Mg}_{(2-2x)}\text{Fe}_{(2x)}\text{SiO}_4$). To learn more about the timescale of the outflows of OH/IR stars, we study the spectral band of crystalline olivine at 69 μm .

Methods. The 69 μm band is of interest because its width and peak wavelength position are sensitive to the grain temperature and to the exact composition of the crystalline olivine. With Herschel/PACS, we observed the 69 μm band in the outflow of 14 OH/IR stars. By comparing the crystalline olivine features of our sample with those of model spectra, we determined the size of the outflow and its crystalline olivine abundance.

Results. The temperature indicated by the observed 69 μm bands can only be reproduced by models with a geometrically compact superwind ($R_{\text{sw}} \lesssim 2500 \text{ AU} = 1400 R_*$). This means that the superwind started less than 1200 years ago (assuming an outflow velocity of 10 km/s). The small amount of mass lost in one superwind and the high progenitor mass of the OH/IR stars introduce a mass loss and thus evolutionary problem for these objects, which has not yet been understood.

Key words. radiative transfer – stars: atmospheres – stars: AGB and post-AGB – stars: evolution – infrared: stars – dust, extinction

1. Introduction

Although still far from a complete theory, the mass loss of asymptotic giant branch (AGB) stars is thought to be triggered by two processes: large-amplitude pulsations and radiation pressure on condensed dust grains (Wood 1979; Castor 1981; Holzer & MacGregor 1985; Bowen 1988; Hearn 1990). Based on stellar evolution models and empirically determined mass loss rates, Vassiliadis & Wood (1993) show that typical AGB stars go through several superwind phases of increased mass loss in which they lose several tenths of a solar mass.

Since the time when Iben & Renzini (1981) introduced the idea of a superwind, many AGB stars were found to have mass loss rates consistent with the suggested superwind values (Knapp & Morris 1985; Bedijn 1987; Wood et al. 1992). The spatial extent of the superwind around oxygen-rich, high mass loss rate OH/IR stars is found to be extremely small. Heske et al. (1990) showed that the mass loss rates derived from CO are lower than those derived from infrared fluxes. And detailed modeling of a sample of stars by Justtanont et al. (2006) and Justtanont et al. (2013) also showed that the mass loss rates derived from SED fitting and by solving the equation of motion for the dust drag wind, are higher than the mass loss rates derived from OH and CO observations. Since the OH and CO emission is from the outer parts of the wind and the dust emission is dominated by more recent mass loss, the authors conclude that a high density superwind indeed exists that has not yet reached the distances where OH and CO lines are formed. Therefore the superwind must have started <2000 years ago. In a detailed study

of the wind of WX Psc, Decin et al. (2007) show that the current superwind phase of WX Psc extends to ~50 AU. Modeling of OH 26.5+0.6 indicated a superwind outflow extending up to ~500 AU (Justtanont et al. 1996; Chesneau et al. 2005; Groenewegen 2012).

OH/IR stars are known to contain moderate abundances of crystalline dust species like crystalline olivine ($\text{Mg}_{(2-2x)}\text{Fe}_{(2x)}\text{SiO}_4$ with x between zero and one, Waters et al. 1996; de Vries et al. 2010; Jones et al. 2012). Theoretical studies predict that the formation of crystalline olivine dust is dependent on the gas density and thus the mass loss rate of the star (Tielens et al. 1998; Gail & Sedlmayr 1999; Sogawa & Kozasa 1999). High densities are more favorable to the formation of crystals than low densities. Even though a temperature contrast makes it difficult to observe crystalline olivine in low mass loss rate AGB stars (Kemper et al. 2001), it is shown that crystalline olivine production increases with the mass loss rate of the AGB star (Jones et al. 2012; Speck et al. 2008). Since the superwind phases of OH/IR stars create a much denser environment, the formation of crystals is expected to be linked with characteristics of the superwind, making the study of crystalline olivine features in the spectra of OH/IR stars interesting.

In this work we introduce a new diagnostic to probe the superwind of OH/IR stars based on the 69 μm spectral band of crystalline olivine. With Herschel/PACS we observed the 69 μm band of crystalline olivine with great sensitivity. This band is of great interest because its width and peak wavelength position are sensitive to the grain temperature and the exact composition of the crystalline olivine Koike et al. (2003); Suto et al. (2006), see

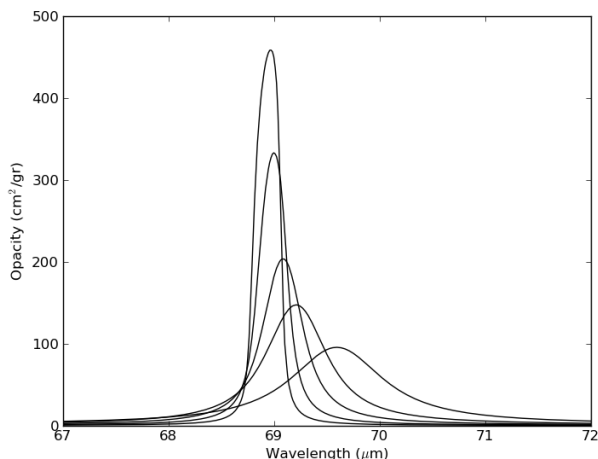


Fig. 1. Opacities of crystalline olivine in the region of the $69\ \mu\text{m}$ band for five different temperatures (pure forsterite, Suto et al. 2006). From the strongest, bluest and most narrow band to the weakest, reddest and broadest band, the opacities are for crystalline olivine with a grain temperature of 50, 100, 150, 200 and 295 K.

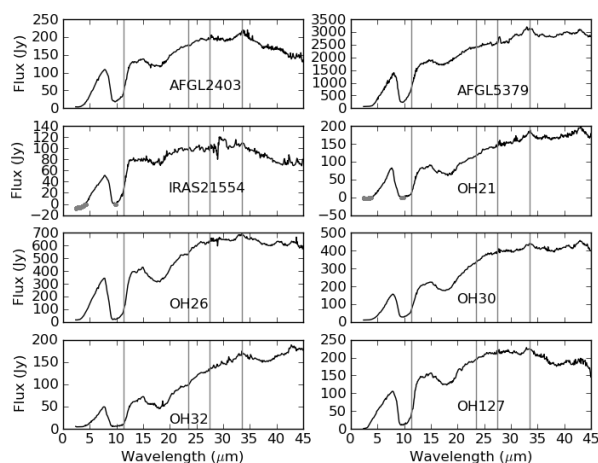


Fig. 2. In black ISO-SWS spectra for the OH/IR stars. The data are taken from Sloan et al. (2003). For the sources OH 21.5+0.5 and IRAS 21554 the flux levels go below zero in regions below $5\ \mu\text{m}$ and in the $9.7\ \mu\text{m}$ band. Those negative flux values are indicated with gray dots. Peaks in the opacity curve of crystalline olivine at 11.3 , 23.5 , 27.5 and $33.5\ \mu\text{m}$ are indicated with vertical g lines.

fig. 1). Because of this temperature dependence the $69\ \mu\text{m}$ band can be used to probe the spatial distribution of the crystalline olivine and thus of the outflow.

In this work we present 14 OH/IR stars which were observed with Herschel/PACS in the wavelength range of the $69\ \mu\text{m}$ band of crystalline olivine (Blommaert et al in prep). We first introduce the sample of stars in sect. 2, describe the spectral features of crystalline olivine in sect. 3 and list the methods used in sect. 4. The modeling is presented in sect. 5, followed by the results in sect. 6. We finish with a discussion and several conclusions in sect. 7.

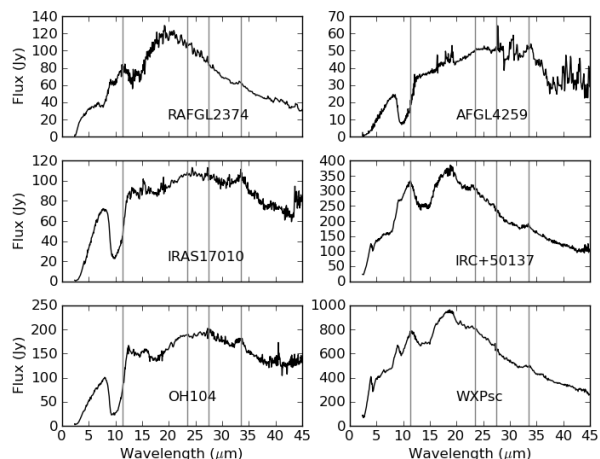


Fig. 3. Continuation of fig. 2

2. Sample selection and data reduction

We selected 14 OH/IR stars based on the presence of crystalline olivine bands in their ISO-SWS spectrum (see fig. 2 and table 1). Crystalline olivine can be best recognized in the ISO-SWS spectra by its emission band at $33.6\ \mu\text{m}$ or by the absorption feature at $11.3\ \mu\text{m}$ on the red wing of the $9.7\ \mu\text{m}$ band of amorphous silicate. See fig. 4 for the opacities of crystalline olivine in the ISO-SWS wavelength range. The central star of the objects in our sample are Galactic disk sources with luminosities going up to several $10,000\ L_{\odot}$ (see table 1, van Langevelde et al. 1990). The central star of the objects is completely obscured by their circumstellar dust shell and their infrared spectrum shows an $9.7\ \mu\text{m}$ absorption band of amorphous silicate. Only WX Psc, RAFGL 2374 and IRC +50137 have their $9.7\ \mu\text{m}$ bands in-between an emission and absorption feature. The infrared spectra of these sources range from relatively blue spectra combined with weak $9.7\ \mu\text{m}$ absorption or emission bands to relatively red spectra with very deep $9.7\ \mu\text{m}$ bands. The blue and red spectra correspond to relatively low ($10^{-6}\ M_{\odot}/\text{yr}$) and high ($10^{-4}\ M_{\odot}/\text{yr}$) mass loss rates respectively. In table 1 the sources are ordered from reddest to bluest from top to bottom.

The observations were taken with the spectrometer Herschel/PACS (Pilbratt et al. 2010; Poglitsch et al. 2010). The objects have been previously published by Blommaert et al. (in prep.) as part of a large sample of observations of the $69\ \mu\text{m}$ band in the spectra of all kinds of evolved stars. For the sources OH 32.8-0.3, OH 30.1-0.7, OH 104.91+2.4 and IRAS 17010 we have spectra in the wavelength range $67\text{--}72\ \mu\text{m}$, which are from the Guaranteed time program "Forsterite dust in the circumstellar environment of evolved stars" (GT1_jblommae_1, Blommaert et al in prep). For the sources OH 21.5+0.5, OH 26.5+0.6, AFGL 2403, IRAS 21554, AFGL 4259, RAFGL 2374, IRC +50137 and AFGL 2019 we also have spectra in the wavelength range of $67\text{--}72\ \mu\text{m}$, which are from the open time program "Study of the cool forsterite dust around evolved stars" (OT2_jblommae_2, Blommaert et al in prep). For the sources OH 127.8+0.0, AFGL 5379 and WX Psc we have full spectral energy distribution Herschel/PACS spectra ($50\text{--}200\ \mu\text{m}$), where OH 127.8+0.0 is a PACS calibration measurement and the other two are from the key program MESS (Groenewegen et al. 2011).

Source name	IRAS	#	\dot{M} ($10^{-5} M_{\odot}/\text{yr}$)	11.3 μm	33.6 μm	69.0 μm	P(days)	L(L_{\odot})
OH 32.8-0.3	18498-0017	1	16 (1)	+	+	+	1,539	23,100
OH 21.5+0.5	18257-1000	2	26 (2)	?	+	+	1,785	72,100-96,900
OH 30.1-0.7	18460-0254	3	18 (3)	+	+	+	2,013	-
OH 26.5+0.6	18348-0526	4	3.2 (4)	+	+	+	1,570	39,362
OH 127.8+0.0	01304+6211	5	9.2 (3)	-	+	+	1,525	38,012
AFGL 2403	19283+1944	6	1.7 (5)	+	+	+	-	1,574
IRAS 21554	21554+6204	7	1.5 (5)	?	+	+	-	4,984
AFGL 5379	17411-3154	8	9.8 (3)	-	+	+	1,440	35,484
OH 104.91+2.4	22177+5936	9	5.6 (6)	-	+	-	1,620	40,871
AFGL 4259	20043+2653	10	-	-	+	-	-	-
IRAS 17010	17010-3840	11	-	+	+	-	-	-
RAFG 2374	19192+0922	12	0.46 (5)	?	+	-	534	4,300
WX Psc	01037+1219	13	1.7 (3)	?	+	-	660	13,914
IRC+50137	05073+52 48	14	0.6 (7)	?	+	-	635	13,284

Table 1. List of the observed OH/IR stars and possible detections of crystalline olivine spectral bands. References for the mass loss rates: (1) Groenewegen (1994), (2) Justtanont et al. (2006), (3) Justtanont et al. (2013), (4) Justtanont et al. (1996), (5) De Beck et al. (2010), (6) Riechers et al. (2005), (7) Justtanont & Tielens (1992). References for the periods and luminosities are van Langevelde et al. (1990) and De Beck et al. (2010) and references therein.

The data reduction of the Herschel/PACS spectra is fully described in Blommaert et al. (in prep.), but is briefly repeated here. The spectra were reduced in the Herschel Interactive Processing Environment (HIPE, Ott 2010) package version 9, using the Herschel/PACS pipe-line script (ChopNodRangeScan.py). The absolute flux calibration used the PACS internal calibration block measurements and for the spectral shape the PACS Relative Spectral Response Function was applied. The PACS integral-field-spectrometer contains 5×5 spatial pixels, the so-called spaxels. The point spread function (PSF) of Herschel is larger than the central spaxel ($9.4'' \times 9.4''$) and a correction needs to be made for the missing part of the PSF, even when combining several spaxels, to obtain the absolute source flux. Because of the pointing accuracy and jitter, it is best to combine as many spaxels under the PSF as possible. However, in order to keep the noise as low as possible, we combined all spaxels with a signal to noise (S/N) larger than 10 rather than blindly adding the central 3×3 spaxels. The S/N of every spaxel is obtained by calculating the standard deviation from a linear fit to the wavelength region of 67.5 to 68.0 μm and dividing this standard deviation by the signal.

The sources AFGL 5379 and OH 21.5+0.5 were pointed off-target. For OH 21.5+0.5 all of the flux was still contained within the 5×5 spaxels and a spectrum could be extracted. The maximum flux within the spaxels for AFGL 5379 was found on one of the border spaxels, and thus not all flux of this object was detected and therefor the flux levels should be taken as a lower limits. We flux calibrated the spectra by calculating the total continuum flux (in the range of 67.5 to 68.0 μm) in the spectrum of all 3×3 spaxels combined and corrected this for the PSF (the flux levels were multiplied with a correction factor of 1.09, see the PACS data reduction manual). This flux value was used to scale the combined spaxels with $S/N > 10$ to the proper continuum flux level.

The ISO-SWS spectra were taken from the Sloan database (Sloan et al. 2003). The ISO-SWS spectra of the sources IRAS 21554 and OH 21.5+0.5 go below zero at wavelengths smaller than 5 μm and in the 9.7 μm band of amorphous silicate. This is probably due to uncertainties in the dark current of the detector (see fig. 2).

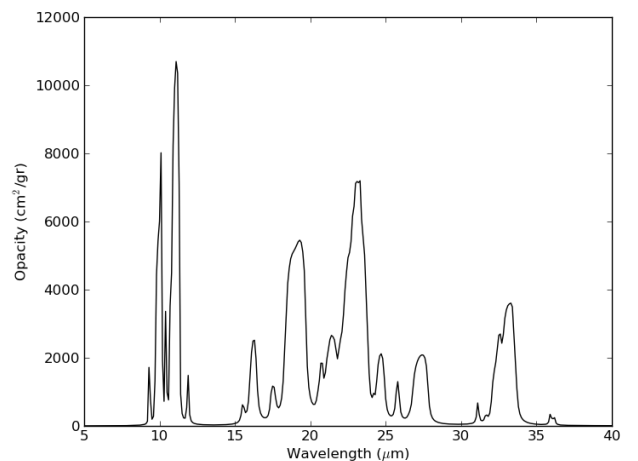


Fig. 4. Opacities of crystalline olivine in the 5-40 μm wavelength range. The opacities are for crystalline olivine with a grain temperature of 150 K and calculated with CDE particle shapes (see sect. 5.1). The optical constants are from Suto et al. (2006).

3. Crystalline olivine spectral features

In this section we describe three key spectral features of crystalline olivine: the 11.3, the 33.6 and the 69.0 μm bands. Figure 4 shows the opacities of crystalline olivine in the 5-40 μm range. For a typical OH/IR star the 11.3 μm band is in absorption on top of the red wing of the 9.7 μm band of amorphous silicate and the 33.6 μm and 69 μm bands are in emission. Between the 11.3 and 33.6 μm bands crystalline olivine also has strong resonances at 23.5 and 27.5 μm , but in the spectra of OH/IR stars these bands are in self-reversal and difficult to discern in the spectra. (see fig. 2 and 3).

The 11.3 μm band

The 11.3 μm band is discussed in de Vries et al. (2010) and they show that when the optical depth of the dust shell is high at these wavelengths, the strength of this band is only dependent on the

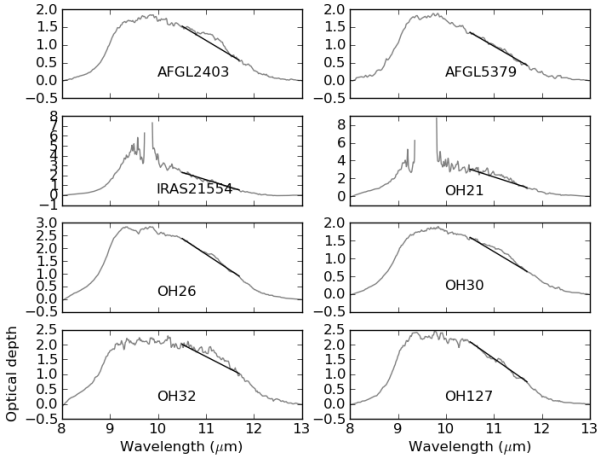


Fig. 5. In gray the optical depth in the region of the $9.7 \mu\text{m}$ band of amorphous silicate. The calculation of the optical depth is described in sect. 4.2 and de Vries et al. (2010). In black the local continuum used under the $11.3 \mu\text{m}$ band. The flux levels of IRAS 21554 and OH 21.5+0.5 go below zero in the region of $9.7 \mu\text{m}$. Those points are not used to calculate the optical depth and are excluded from these plots.

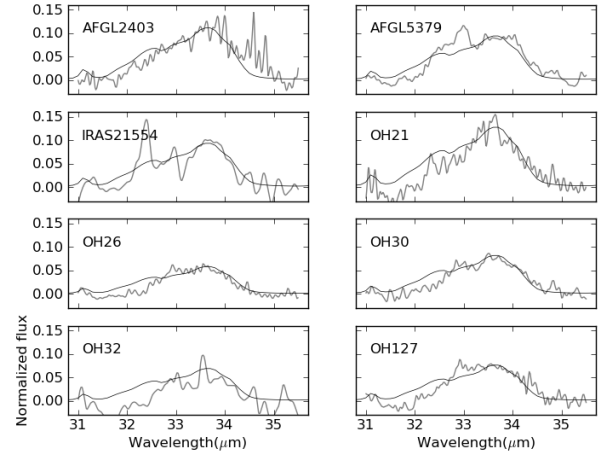


Fig. 7. Normalized $33.6 \mu\text{m}$ bands derived from the spectra in the Sloan database (Sloan et al. 2003). The normalization is done by calculating $(F/F_{\text{continuum}}) - 1$. The scale of the y-axis is the same for all plots. In black are plotted the opacities of crystalline olivine (at 150 K, using CDE, see sect. 5.1). The opacities are normalized to the level of the observed band in the range of $33.4\text{--}33.6 \mu\text{m}$.

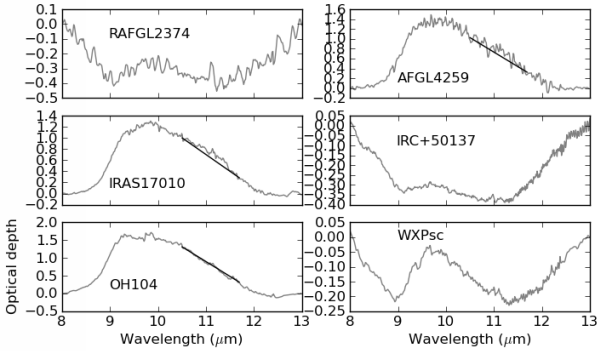


Fig. 6. Continuation of fig. 5

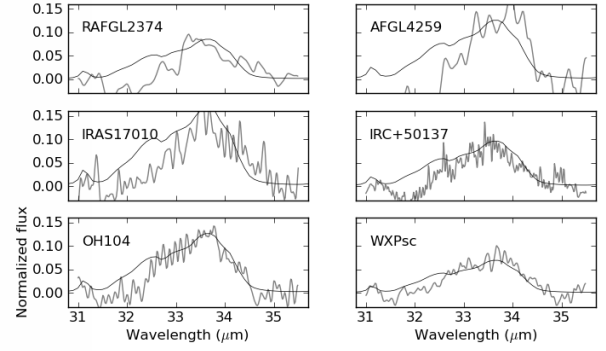


Fig. 8. Continuation of fig. 7.

crystalline olivine abundance and not on other properties of the dust shell or central star. The $11.3 \mu\text{m}$ band probes the material close to the central star and in the line of sight to the central star. The presence of a $11.3 \mu\text{m}$ band can be best seen in plots of the optical depth shown in figures 5 and 6. For the three stars with $9.7 \mu\text{m}$ bands that are in-between an emission and absorption band (RAFL 2374, WX Psc, IRC +50137) we could not measure the $11.3 \mu\text{m}$ band, indicated with a "?" in table 1. The sources OH 21.5+0.5 and IRAS 21554 have ISO-SWS spectra that go below zero in the $9.7 \mu\text{m}$ band of amorphous olivine and because of this we do not analyze the $11.3 \mu\text{m}$ bands of these sources (also indicated with a "?" in table 1). Among the sources that have a detected $69 \mu\text{m}$ band we find that OH 32.8-0.3, OH 30.1-0.7, OH 26.5+0.6 and AFGL 2403 also show a $11.3 \mu\text{m}$ band. For the objects OH 127.8+0.0 and AFGL 5379 we do not detect an $11.3 \mu\text{m}$ band while they do show a $69 \mu\text{m}$ band. Among the sources without detected $69 \mu\text{m}$ bands we only find an $11.3 \mu\text{m}$ band for IRAS 17010.

The $33.6 \mu\text{m}$ band

Figure 7 and 8 show the continuum divided $33.6 \mu\text{m}$ bands of the 14 OH/IR stars. Because the band is easily recognized in the spectra and was used to select the sample, we considered using it for our quantitative analysis. However, we found this is not trivial. First because many of these bands show a double peaked profile for the $33.6 \mu\text{m}$ band, indicating it is probably a blend of more than one spectral band. Which other dust species is present in this spectral feature is not clear. And secondly, de Vries et al. (2010) showed that the observed strength of the $33.6 \mu\text{m}$ band in OH/IR type stars is dependent on many of the properties of the dust shell, since the optical depth at this wavelength is already larger than one. In this study we use the $33.6 \mu\text{m}$ band to determine the presence of crystalline olivine, but because the band has a complicated structure and is strongly dependent on the outflow parameters, we do not use this band quantitatively in any further analysis.

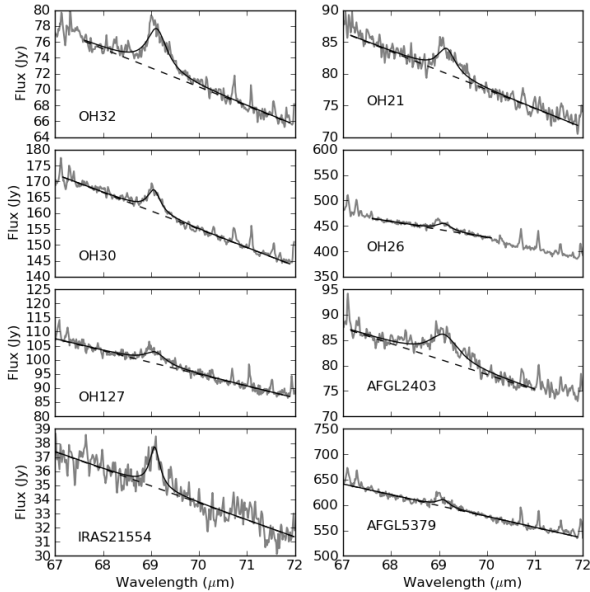


Fig. 9. In gray Herschel/PACS spectra for the OH/IR stars with 69 μm crystalline olivine band detections. In dashed and solid black the fitted continuum and fitted Lorentzian profile.

The 69 μm band

For the reddest and most obscured sources in our sample, we detected the 69 μm band, but for the six bluest and lowest mass loss rate sources in our sample we did not (see fig. 9 and 10). Already by eye it can be seen that the 69 μm band of IRAS 21554 is the narrowest and the one of AFGL 2403 the broadest.

The weakest, but still detected 69 μm bands, are seen in the spectrum of OH 26.5+0.6 and AFGL 5379, which also have weak and almost undetectable 11.3 μm bands. The sources OH 32.8-0.3, AFGL 2403, OH 21.5+0.5 and IRAS 21554 show very strong 69 μm bands. For OH 32.8-0.3 and AFGL 2403 we indeed also detect strong 11.3 μm bands. The 11.3 μm bands of OH 21.5+0.5 and IRAS 21554 are difficult to analyze because of their uncertain ISO-SWS flux levels. For the six sources that do not have detected 69 μm bands we also do not find 11.3 μm bands, or we can not see them because of the self reversal of the 9.7 μm band. Only IRAS 17010 has a convincing detection at 11.3 μm while having none at 69 μm .

Most sources show gas lines in the Herschel/PACS range, which can be attributed to species like ortho- and para- H_2O , ^{12}CO , ^{28}SiO , and SO_2 (Decin 2012, Blommaert et al in prep.). A blend of gas lines, although weak, is situated on top of the 69 μm band. There are only three sources in our sample for which we do not detect these gas lines: IRAS 21554, AFGL 4259 and IRAS 17010.

4. Method and observational diagrams

In this study we want to answer specific questions regarding the distribution of crystalline olivine in the circumstellar environment of OH/IR stars. We can quantitatively determine how much and where the crystalline olivine is in the circumstellar environment by studying the two spectral features at 11.3 and 69 μm . In this section we discuss which properties of these bands are used,

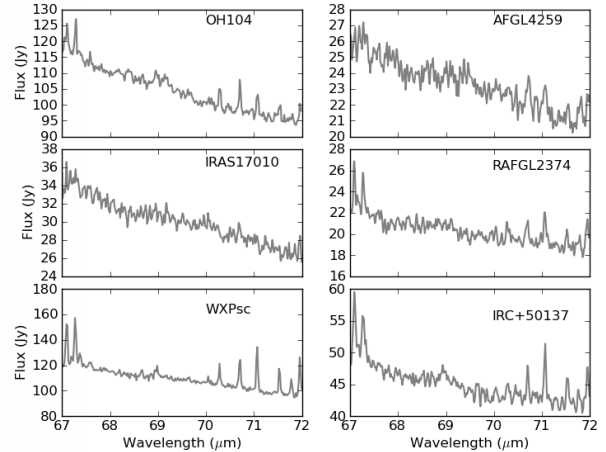


Fig. 10. Continuation of fig. 9

how we measure them and see how they relate to each other. In sect. 6 we compare the properties of the observations with those of models.

4.1. Selection of spectral properties and motivation

As a probe of the spatial distribution of the crystalline olivine material we take the width of the 69 μm band. The width of this band is sensitive to the grain temperature of the crystalline olivine and thus to the temperature gradient of crystalline olivine in the circumstellar environment. Using the models in sect. 5 we indeed show that the width of the 69 μm band can be used to determine up to what radius crystalline olivine is present in the circumstellar environment. The sources in our sample are all outflow sources and if the distribution of crystalline olivine is the same as the distribution of the other dust species, the width of the 69 μm band is a probe of the size of the outflow and also of the timescale of the outflow. The width of the 69 μm band could also depend on other parameters like the mass loss rate and we investigate these possible dependencies in sect. 5.

We also measure the peak-over-continuum strength of the 69 μm band. The strength of this band is, among others, dependent on the abundance of the crystalline olivine. Because the wavelength position of the band is at such long wavelengths, all the line of sights probe deep into the outflow and the abundance derived from the strength of the 69 μm band is representative of the average abundance in the whole outflow. This is in contrast to what de Vries et al. (2010) have shown for the strength of the 11.3 μm band. de Vries et al. (2010) define the strength of the 11.3 μm band as:

$$S_{11.3} = \int \left(\frac{\tau_{\text{cr}}}{\tau_{\text{all}}} - 1 \right) d\lambda \quad (1)$$

Where the integral $d\lambda$ sums over the spectral feature and τ_{cr} and τ_{all} are the optical depth of crystalline olivine only and the optical depth of all dust species together, respectively. In the optical thick limit, equation 1 can be approximated by:

$$S_{11.3} = \int \int \left(\frac{\rho(R) \times A_{\text{cr}} \times \kappa_{\text{fo}}}{\rho(R) \times \kappa_{\text{all}}} - 1 \right) dV d\lambda \propto A_{\text{cr}} \quad (2)$$

Where $\rho(R)$ is the density in the outflow, A_{cr} the abundance of crystalline olivine and κ_{cr} and κ_{all} the opacity of only crystalline olivine and that of all dust species together, respectively. The integral $d\lambda$ sums over the spectral feature, while dV sums over the volume of the outflow. In order to make the last step we assume that the crystalline olivine abundance is constant throughout the outflow. de Vries et al. (2010) have indeed shown that if the optically thick limit holds, the strength of the $11.3 \mu\text{m}$ band is only dependent on the abundance of crystalline olivine in the line of sight. They show that the optically thick regime is valid when the mass loss rate is higher than $\sim 5 \cdot 10^{-5} M_{\odot}/\text{yr}$ (with a gas to dust ratio of 100). This shows that in the optically thick regime, the strength of the $11.3 \mu\text{m}$ band is a good probe of the abundance of crystalline olivine in the line of sight and close to the central star. The combination of the strength of the $11.3 \mu\text{m}$ band and the strength of the $69 \mu\text{m}$ band are therefore a good probe of a spatial abundance gradient in the circumstellar material.

In this study we determine the distribution of crystalline olivine from its spectral features and do not aim to determine the properties of the amorphous dust or mass loss rates from the SED. But we still want to have a quantitative measure of the color of the SED in order to compare it with the properties of the 11.3 and $69 \mu\text{m}$ bands. In order to characterize the color of the SED we measure the flux ratio $F(30 \mu\text{m})/F(18 \mu\text{m})$. Several of our sources with the bluest SEDs of our sample have flux values with $F(30 \mu\text{m}) < F(18 \mu\text{m})$ (for example WX Psc or RAFGL 2374, see fig. 2 and 3). And other stars have very red SEDs with $F(30 \mu\text{m}) > F(18 \mu\text{m})$, like for example OH 26.5+0.6 or OH 21.5+0.5.

4.2. Measuring the spectral properties

Measuring the $11.3 \mu\text{m}$ band

We briefly describe how we measured the strength of the $11.3 \mu\text{m}$ band and the reader is referred to de Vries et al. (2010) for the details. As shown in equation 1, the strength of the $11.3 \mu\text{m}$ band is calculated as the ratio of the optical depth due to only crystalline olivine (τ_{cr}) and the optical depth of all dust species (τ_{all}). We first construct a continuum over the $9.7 \mu\text{m}$ band of amorphous olivine. The optical depth in the $9.7 \mu\text{m}$ band is calculated using $\tau = -\ln(F/F_{\text{cont}})$, where F_{cont} is the flux level of the continuum constructed over the $9.7 \mu\text{m}$ band of amorphous silicate. Figure 5 and 6 show the optical depth in the $9.7 \mu\text{m}$ band for the sources in this study. The optical depth in the $9.7 \mu\text{m}$ band due to crystalline olivine (τ_{cr}) and due to the other dust species (τ_{all}) is now determined by constructing a continuum in τ -space, under the $11.3 \mu\text{m}$ band (for examples see fig. 5 and 6). The strength of the $11.3 \mu\text{m}$ band is now calculated by integrating over the $11.3 \mu\text{m}$ band as shown in equation 1.

The two sources OH 127.8+0.0 and AFGL 5379 have no $11.3 \mu\text{m}$ bands that we could identify by eye (see table 1 and fig. 5). But even though we do not recognize the feature, we applied the calculation of the $11.3 \mu\text{m}$ band to these sources and treat the measured values as upper limits for the strength of the $11.3 \mu\text{m}$ band, see sect. 4.3.

Measuring the $69 \mu\text{m}$ band

The observations are fitted over the range of $67\text{--}72 \mu\text{m}$ with a Lorentzian together with a slightly curved continuum (second order polynomial, see figures 9 and 10). Most of the OH/IR stars show gas lines in their spectra and we excluded the following wavelength regions in our fits (all in μm): $66.9\text{--}67.15$; 67.22--

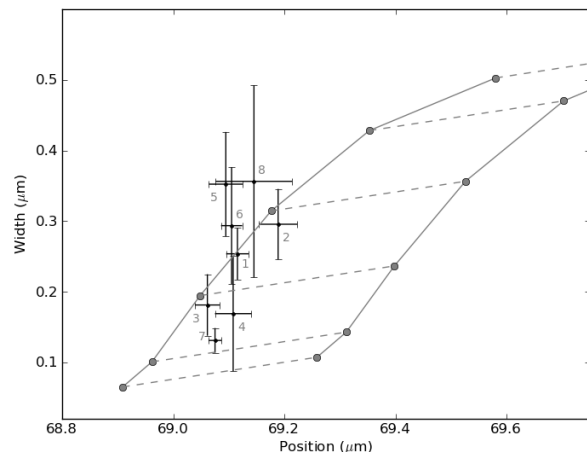


Fig. 11. The width and position of the observed $69 \mu\text{m}$ bands are plotted against each other in black dots. Gray solid and dashed lines are the width and position of $69 \mu\text{m}$ bands from laboratory measurements and interpolations between them at different temperatures and compositions. The left solid gray curve is for crystalline olivine with 0% iron and with temperatures going from 50, 100, 150, 200, 295 K for the narrowest to broadest features. The right solid gray curve is for the same temperatures but for crystalline olivine with 1% iron (based on the interpolations of de Vries et al. 2012). Dashed gray lines connect points with the same temperature.

67.41 ; $67.47\text{--}67.6$; $68.91\text{--}69.02$; $70.6\text{--}70.8$; $71.0\text{--}71.15$; $71.5\text{--}71.6$ and $71.9\text{--}72.2$.

The peak-over-continuum strength is obtained by dividing the amplitude of the Lorentzian fit by the continuum flux at the peak wavelength position of the feature. For stars without a detection at $69 \mu\text{m}$ we determined an upper limit for the peak-over-continuum strength of the band. To do this we made a linear fit to the wavelength range $67.5\text{--}68.2 \mu\text{m}$ in the Herschel/PACS spectrum and took the standard deviation of the flux relative to this continuum as an upper limit of the peak-over-continuum strength of the $69 \mu\text{m}$ band.

Quantitative measure of the color of the spectrum

The fluxes at 18 and $30 \mu\text{m}$ for the flux ratio $F(30 \mu\text{m})/F(18 \mu\text{m})$ are calculated from the ISO-SWS spectra by taking the average in the regions $17.5\text{--}18.5$ and $29.5\text{--}30.5 \mu\text{m}$, respectively.

Error calculation

The errors on the width, position and strength of the $69 \mu\text{m}$ band and the strength of the $11.3 \mu\text{m}$ band are obtained by a Monte Carlo method. The error on the properties of the bands are calculated by repeating the analysis of the bands multiple times, while randomly varying (by $\pm 0.02 \mu\text{m}$ from the standard value) the wavelength location of the fitting borders, the borders of the continuum and the wavelength location of the gas lines that are excluded. The standard deviation of the sample of fitting results is then taken as the error.

4.3. Observational diagrams

We summarize the properties of the $11.3 \mu\text{m}$ and $69 \mu\text{m}$ bands and the color of the spectrum with five diagnostic diagrams. The

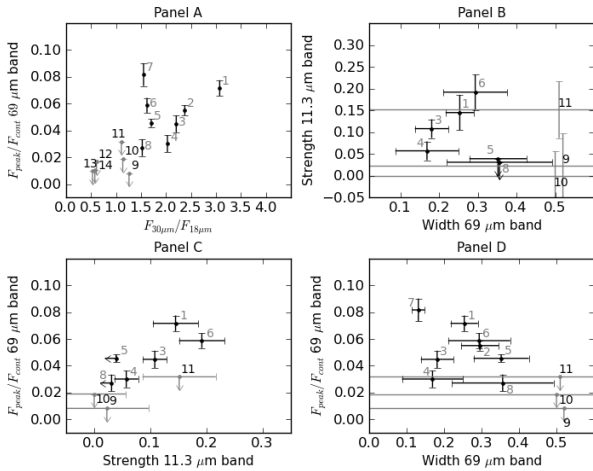


Fig. 12. The panels show different properties of the observed spectra. The observations are plotted in black and gray dots for the observations with and without detected $69\ \mu\text{m}$ bands respectively. In panel A is plotted the peak-over-continuum strength of the $69\ \mu\text{m}$ band versus the $F_{30\mu\text{m}}/F_{18\mu\text{m}}$ color of the spectrum. In panel B the strength of the $11.3\ \mu\text{m}$ band is plotted against the width of the $69\ \mu\text{m}$ band. In panel C the peak-over-continuum strength of the $69\ \mu\text{m}$ band and the strength of the $11.3\ \mu\text{m}$ band are shown. The peak-over-continuum strength of the $69\ \mu\text{m}$ band is plotted against the width of the $69\ \mu\text{m}$ band in panel D.

first diagram shows the width plotted against the position of the $69\ \mu\text{m}$ bands (see fig. 11). The width and position of the laboratory measurements of the $69\ \mu\text{m}$ bands shown in gray in fig. 11 are based on the data sets of Suto et al. (2006) and Koike et al. (2003). All details about how these curves are generated from the laboratory measurements are explained in de Vries et al. (2012). From fig. 11 it can be seen that the observations have positions and widths close to the curve of crystalline olivine with 0% iron and with grain temperatures ranging from 100–200 K.

Figure 12A shows the peak-over-continuum strength of the $69\ \mu\text{m}$ band as a function of the color of the spectrum. Besides the source IRAS 21554 (#7), all sources follow a diagonal trend where the $69\ \mu\text{m}$ band becomes stronger as the spectrum becomes redder. This is an important diagram because it shows that the emission from the crystalline olivine is related to the overall emission of the dusty outflow.

Panel B from fig. 12 shows the strength of the $11.3\ \mu\text{m}$ band plotted against the width of the $69\ \mu\text{m}$ band. Even though the sources seem to scatter over the diagram, this diagram is very useful in reading of the crystalline olivine grain temperature from the width of the $69\ \mu\text{m}$ band and the crystalline olivine abundance in the line of sight from the $11.3\ \mu\text{m}$ band. The diagram shows that the abundance of crystalline olivine in the line of sight does not correlate with the crystalline olivine grain temperature (which is a probe of the extent of the outflow, see sect. 5).

In fig. 12C we plot the peak-over-continuum strength of the $69\ \mu\text{m}$ band versus the strength of the $11.3\ \mu\text{m}$ band. This diagram is important because if the $11.3\ \mu\text{m}$ and the $69\ \mu\text{m}$ band come from the same population of crystalline olivine dust we expect these two bands to correlate with each other. The diagram indeed shows that the strength of the $69\ \mu\text{m}$ band increases as the strength of the $11.3\ \mu\text{m}$ band increases.

As a last diagram we also plot the strength of the $69\ \mu\text{m}$ band against the width of the $69\ \mu\text{m}$ band in fig. 12D. This diagram

Dust species	Reference
Amorphous olivine (Mg_2SiO_4)	Jäger et al. (1998)
Amorphous olivine (MgFeSiO_4)	Jäger et al. (1998)
Metallic iron (Fe (solid))	Ordal et al. (1988)
Crystalline olivine (Mg_2SiO_4)	Suto et al. (2006)

Table 2. Dust species used in this paper and references to the used optical constants

can be used to investigate whether the abundance, that can be deduced from the $69\ \mu\text{m}$ band, correlates with the grain temperature of crystalline olivine (which is a probe of the extent of the outflow). A weak anti-correlation can be seen between the peak-over-continuum strength and the width of the $69\ \mu\text{m}$ band. This can be understood since a smaller width means colder crystalline olivine and a more strongly peaked $69\ \mu\text{m}$ band. But we need to mention that the strength of the $69\ \mu\text{m}$ band is not only depend on the temperature, but also on the abundance of the crystalline olivine. In sect. 5 we investigate all the different properties that have an effect on the strength of the $69\ \mu\text{m}$ band

5. Modeling

In this section we introduce a grid of models to interpret the observed crystalline olivine spectral features.

5.1. Radiative transport and dust properties

Model spectra were computed using the Monte Carlo radiative transport code MCMax (Min et al. 2009). Within the code we treat AGB stars as a central star enclosed in a spherically symmetric dust shell. The central star is treated as a black body and defined by its radius and temperature (see table 3). We used a typical stellar temperature of 2700 K and luminosity of $7000\ L_\odot$ (Habing & Olofsson 2003). This gives a radius for the central star of $380\ R_\odot = 1.8\ \text{AU}$.

For the dust-to-gas ratio a value of 1/100 is assumed. The mass loss rate values mentioned in this paper always refer to the total (dust and gas) mass loss rates, assuming this dust-to-gas ratio. The temperature of the dust shell reaches a value of 1100 K at a radius of $\sim 8\ \text{AU}$. For all dust species this radius is taken to be the radius at which the dust species condense, and therefore defines the inner radius of the dust shell. By doing this we assume that the dust species formed before this 1100 K limit have a negligible effect on the spectrum. This is especially true for the optically thick dust shells where the infrared spectrum is not sensitive anymore to changes in the inner part of the dust shell. The terminal wind speed (v_{exp}) is set to the typical value of 10 km/s. In our modeling we use a density distribution proportional to r^{-2} , meaning that changes in the terminal wind speed only scale the mass loss rate values, but not change the model results.

The outflows of oxygen-rich AGB stars are mainly composed out of amorphous silicate dust. A moderate amount of crystalline silicates and metallic iron can be present. For the amorphous dust we use amorphous olivine ($(\text{Mg}, \text{Fe})_2\text{SiO}_4$). We use two laboratory measurement sets for the amorphous olivine: Mg_2SiO_4 and MgFeSiO_4 (see table 2). We can combine different ratios of these two amorphous olivines to simulate different amorphous olivine compositions. As a smooth continuum opacity we use metallic iron (Kemper et al. 2002). We also include crystalline olivine with zero percent iron.

In our modeling we did not consider composite grains, such as grains that share a physical connection and thus their tem-

perature. We do not consider composite grains because in these optically thick environments, the temperature of all dust species converges to the same value. The reason for different dust particles in the wind to reach the same temperature in an optically thick wind is that the absorption and emission of the grains happens at the same wavelength. In an optically thick wind the radiation field a dust particle can absorb is dominated by the infrared radiation of the surrounding dust grains. This contrasts to an optically thin wind, where absorption and emission can happen at different wavelengths and dust particles of different sizes or compositions can thus reach different temperatures. In such optically thin winds the radiation field that is absorbed by a dust grain is dominated by the radiation field of the central star, while the dust grain radiates at infrared wavelengths.

The optical constants used for these dust species are listed in table 2. We use the continuous distribution of ellipsoids (Bohren & Huffman 1983) shape distribution for the dust particles, which is valid for grains small compared to the wavelength of interest. The dust grains in the outflow of AGB stars are found not to exceed $\sim 1 \mu\text{m}$ (Norris et al. 2012), making the CDE distribution applicable. We would like to note that the $69 \mu\text{m}$ band is independent of the grain size or shape distribution when small grains are considered ($< 3.0 \mu\text{m}$, de Vries et al. 2012; Sturm et al. 2013).

The code MCMMax handles temperature dependent opacities by using different opacity curves for the same dust species at different temperatures. For temperatures in between those temperatures for which opacity curves are available, MCMMax interpolates between the two opacity curves. For temperatures above or below that for which opacity curves are available, MCMMax uses the opacity curve for the highest or lowest temperature available, respectively. MCMMax iterates to see if the opacities change the temperature structure in the shell and it updates the opacities at every iteration.

In the outflow of OH/IR stars the temperature of the crystalline olivine grains can span a range from up to 1100 K at the condensation radius and down to 5 K or lower at the connection of the outflow to the ISM. For crystalline olivine (with no iron, $x=0$) optical constants are only available at 50, 100, 150, 200 and 295 K (Suto et al. 2006). From these data sets we know that at higher temperatures the $69 \mu\text{m}$ band will eventually be so weak and broad that it is indistinguishable from the continuum (see fig. 1). Since the OH/IR stars we study contain at least some dust at these high temperatures, it could be important to take this into account. We have tested to see if it had an effect if we assume that at 600 K the crystalline olivine band at $69 \mu\text{m}$ has completely disappeared (while the other features are still the same as for 295K). We found that it did not matter for the properties of the crystalline olivine bands. The reason is that the crystalline olivine dust with temperatures much higher than 300 K are in the inner parts of the outflow (within the $\tau \sim 1$ area) and therefore do not directly contribute to the spectrum.

5.2. Outflow parameters

We assume the star is currently in its superwind phase and has an enhanced mass loss reaching out to a radius of R_{SW} from the central star. This means that this superwind started $R_{\text{SW}}/v_{\text{exp}}$ years ago, where v_{exp} is the expansion velocity of the outflow. At radii outside R_{SW} and up to R_{out} , an older outflow is present expelled before the superwind and at a mass loss rate a factor Φ lower than that of the superwind. We take 500,000 AU as the outer radius because at this point the outflow has transitioned into the interstellar material. The dust shell reaches temperatures below 5 K at radii of 500,000 AU. Due to the interstellar radiation field

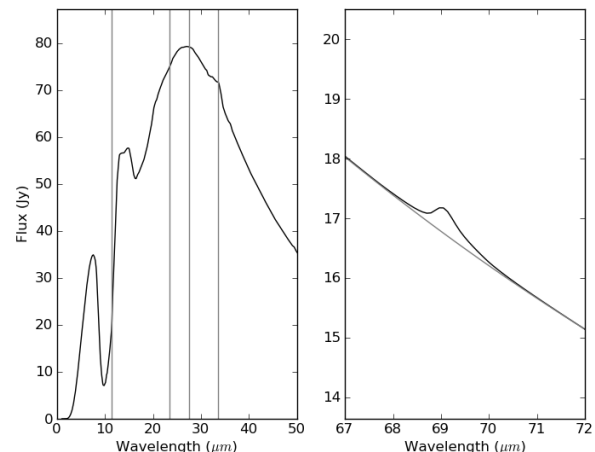


Fig. 13. Standard model spectra in the range of 2-50 μm and 67-72 μm . For parameters see table 3. In gray the continuum under the $69 \mu\text{m}$ band. Spectral bands of crystalline olivine at 11.3, 23.5, 27.5 and $33.5 \mu\text{m}$ are indicated with vertical gray lines. The 23.5 and $27.5 \mu\text{m}$ bands are difficult to detect because these spectral bands are already in self reversal.

the temperature of the outer radius of the dust shell could be significantly higher, for example Li & Draine (2001) show that the temperature at the outer edge can be as high as 20 K or higher. Which outer radius is chosen is of no consequence to our results, since we show that this outer radius is of no influence on the properties of the $11.3 \mu\text{m}$ and $69 \mu\text{m}$ bands (see section 5.4).

Within the superwind and in the pre-superwind mass loss we assume that the density distribution of our models is spherically symmetric and time independent with an r^{-2} radial dependence. In our modeling approach we test the effect of the R_{SW} , Φ , R_{out} and the mass loss rate on the spectral features. From here on, mentioned mass loss rates always refer to that of the superwind. We also test the effects of the composition of the amorphous olivine, the metallic iron abundance and crystalline olivine abundance.

For the spatial distribution of the crystalline olivine we consider two cases. The first is that the crystalline olivine is only present in the superwind part of the outflow. This situation is expected, since crystalline material forms more efficiently in higher density regions (Tielens et al. 1998; Gail & Sedlmayr 1999; Sogawa & Kozasa 1999; Jones et al. 2012). In the second, the crystalline olivine is present in both the superwind and the pre-superwind mass loss.

We also test if we can detect whether an OH/IR star has gone through one or several superwind phases. In our models the star is currently in a superwind phase, but we also test how the spectrum changes if another previously emitted superwind outflow is present.

5.3. Standard model

In order to visualize the effects of all the parameters we define a standard model for which we change one parameter at a time and investigate the changes (see table 3). For our standard model we take a typical superwind with a radius of 500 AU and a mass loss rate of $5 \cdot 10^{-5} M_{\odot} \text{yr}^{-1}$. The mass loss rate observed for OH/IR stars ranges between $1 \cdot 10^{-5} M_{\odot} \text{yr}^{-1}$ and up to $15 \cdot 10^{-5} M_{\odot} \text{yr}^{-1}$

Standard model parameters

mass loss rate ($10^{-5} M_{\odot} \text{ yr}^{-1}$)	5
Inner radius (AU)	8
Superwind radius (R_{SW} , AU)	500
Ratio of old to superwind mass loss (Φ)	0.1
Outer radius dust shell (AU)	500,000
Luminosity central object (L_{\odot})	7,000
Temperature central object (K)	2,700
Radius central object (R_{\odot})	385
Terminal velocity (v_{exp} , km/s)	10
<i>Dust abundances (% by mass):</i>	
Amorphous olivine	92
Metallic iron	4
Crystalline olivine	4
<i>Dust composition:</i>	
Amorphous olivine ($\frac{\text{Amount}(\text{Mg}_2\text{SiO}_4)}{\text{Amount}(\text{MgFeSiO}_4)}$)	0.5
Metallic iron	Fe (solid)
Crystalline olivine	Mg_2SiO_4
Dust shape model	CDE
Location of the crystalline olivine	$< R_{\text{SW}}$

Table 3. Standard model parameters.

(Chesneau et al. 2005; Riechers et al. 2005; Justtanont et al. 1996; Schutte & Tielens 1989; Groenewegen 1994).

It is not quite clear what the difference in mass loss rate is between the superwind and the pre-superwind phase. Modeling done in different studies on the same object (OH 26.5+0.6) resulted in different Φ values of 1/500 to 1/5 (Justtanont et al. 1996; Chesneau et al. 2005; Groenewegen 2012). Justtanont et al. (2013) find a typical Φ value of the order ~ 0.01 for the objects OH 127.8+0.0, WX Psc, AFGL 5379, OH 26.5+0.6 and OH 30.1-0.7. As a standard value we take the old mass loss rate emitted before the superwind a factor of 10 ($\Phi = 0.1$) lower than that of the superwind. We describe the effect of this parameter in sect. 5.4.

Crystalline olivine abundances in OH/IR stars can vary from less than 2% to higher than 10% (de Vries et al. 2010) and we choose a value of 4% for our standard model. For the distribution of the crystalline olivine in the outflow we assume the crystalline olivine is only present in the superwind. Our standard model is currently in a superwind phase and in the standard model we do not include any previously emitted superwind. For the metallic iron abundance we take an abundance of 4%, which is in the order of what Kemper et al. (2002) found for OH 127.8+0.0. The infrared spectrum of the standard model can be viewed in fig. 13. It is a model spectrum that displays the basic properties of observed OH/IR spectra in that it shows a clear $9.7 \mu\text{m}$ absorption band of amorphous olivine, that it peaks at wavelength longer than $20 \mu\text{m}$ and that it shows crystalline olivine bands at 33.6 and $69 \mu\text{m}$.

5.4. Modeling results

In this section we show the effects of different parameters on the infrared spectrum and its crystalline olivine spectral features.

Superwind radius and mass loss rate

We test three radii for the superwind: 200, 500 and 2500 AU and we test these superwind radii at four different mass loss rates: $1 \cdot 10^{-5} M_{\odot}/\text{yr}$, $5 \cdot 10^{-5} M_{\odot}/\text{yr}$, $10 \cdot 10^{-5} M_{\odot}/\text{yr}$ and $15 \cdot 10^{-5} M_{\odot}/\text{yr}$.

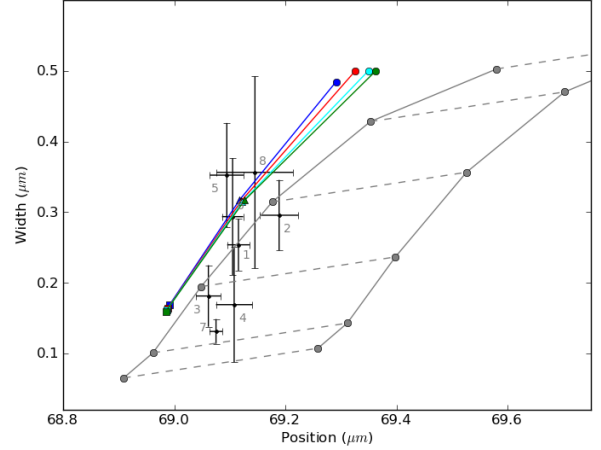


Fig. 14. The blue, red, teal and green curves are for model $69 \mu\text{m}$ bands with mass loss rates of $1 \cdot 10^{-5} M_{\odot}/\text{yr}$, $5 \cdot 10^{-5} M_{\odot}/\text{yr}$, $10 \cdot 10^{-5} M_{\odot}/\text{yr}$ and $15 \cdot 10^{-5} M_{\odot}/\text{yr}$, respectively. The circle, triangle and square are for superwind radii of 200, 500 and 2500 AU, respectively. All other model parameters are listed in table 3. The width and position of the observed $69 \mu\text{m}$ bands are plotted with black dots. Gray solid and dashed lines are as in fig. 11.

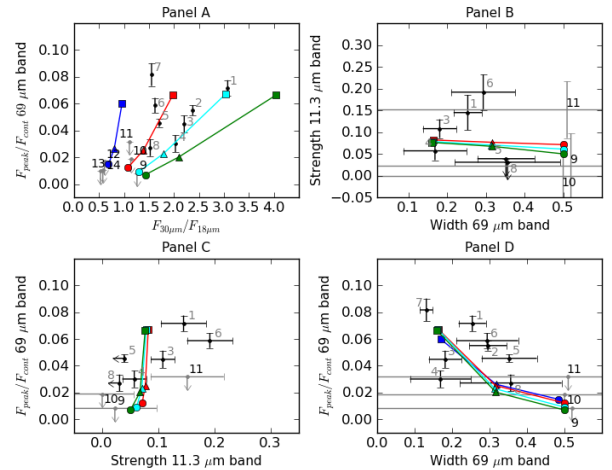


Fig. 15. The panels show different properties of model and observed spectra. The circle, triangle and square markers indicate models with **superwind radii** of 200, 500 and 2500 AU respectively. The blue, red, teal and green curves are for models with mass loss rates of $1 \cdot 10^{-5} M_{\odot}/\text{yr}$, $5 \cdot 10^{-5} M_{\odot}/\text{yr}$, $10 \cdot 10^{-5} M_{\odot}/\text{yr}$ or $15 \cdot 10^{-5} M_{\odot}/\text{yr}$ respectively. All other model parameters are listed in table 3. The observations are shown as in fig. 12.

Fig. 14 shows that the position and width of the $69 \mu\text{m}$ band are not dependent on the mass loss rate for superwind radii larger than 200 AU. From fig. 14 it is also clear that less extended superwinds have crystalline olivine bands at $69 \mu\text{m}$ that are dominated by warmer grain temperatures than superwinds with larger radii.

Figure 14 shows that the width and position of model $69 \mu\text{m}$ bands are broader than those of the laboratory measurements. This is because there is a temperature gradient in the outflow, making the $69 \mu\text{m}$ band a superposition of $69 \mu\text{m}$ bands of

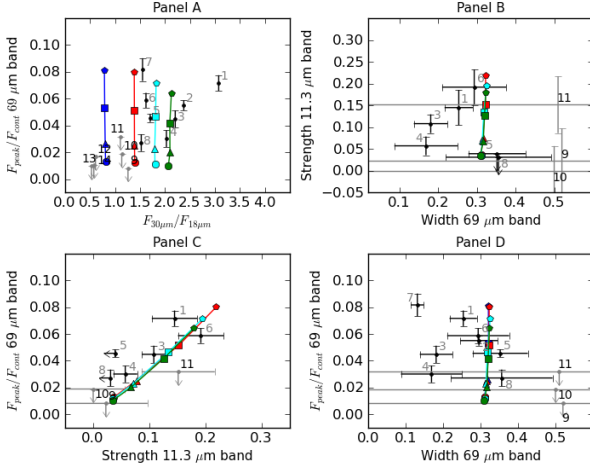


Fig. 16. The panels show different properties of model and observed spectra. The circle, triangle and square markers indicate models with **crystalline olivine abundances** of 2%, 4% and 8% respectively. The other properties are as in fig. 15.

different temperatures, effectively broadening the band. It further seems that the observations with narrower bands (#3, 4 and 7) lay further away from the model bands than those with broader widths (among which #5, 6 and 8). This could mean that the crystalline olivine in superwinds with larger radii contain slightly more iron.

Figure 15 shows the four panels with different spectral characteristics plotted against each other for models with varying superwind radii and mass loss rates. Panel A shows that the color of the spectrum becomes redder when the mass loss rate and/or the superwind radius increases. The peak-over-continuum strength of the 69 μm band is not strongly dependent on the mass loss rate, but is strongly influenced by the superwind radius. Panel B, C and D show that the strength of the 11.3 μm band is not dependent on the mass loss rate nor the superwind radius. The width of the 69 μm band on the other hand is a strong function of the superwind radius, but independent of the mass loss rate.

Crystalline olivine abundance

Figure 16 shows models with different crystalline olivine abundances. It is clear that the abundance has no influence on the color of the spectrum or the width of the 69 μm band. What it does influence is the strength of the 11.3 and 69 μm bands. Because the crystalline olivine abundance has no effect on the width and position of the 69 μm band, no diagram like fig. 14 is shown for this parameter.

Pre-superwind mass loss

We have investigated the effect of the strength of the mass loss emitted prior to the superwind phase, by changing the parameter Φ . By default Φ is set to 0.1, but here we also test the values 0.0 and 0.5. The $\Phi = 0$ model corresponds to no mass loss prior to the superwind and $\Phi = 0.5$ to a pre-superwind mass loss rate with a rate half that of the superwind. Note that in our standard model we do not include crystalline olivine in the pre-superwind mass loss phase. Figure 17 shows that for Φ is 0.0 or 0.1 there is no significant change in any of the characteristics. In order to

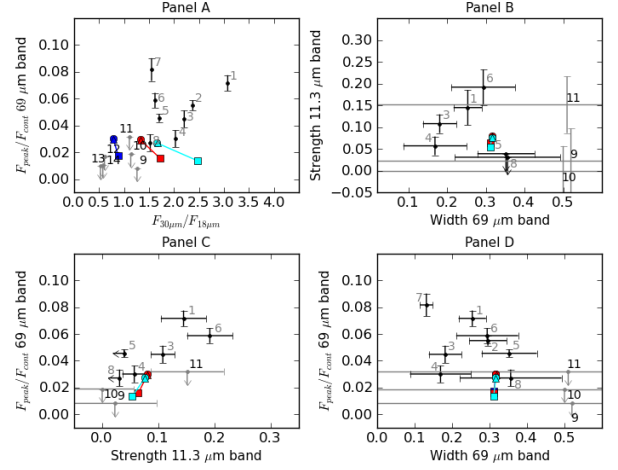


Fig. 17. The panels show different properties of model and observed spectra. The circle, triangle and square markers indicate models with **pre-superwind mass loss rate** fractions (Φ) of 0.0, 0.01 and 0.5 respectively. The other properties are as in fig. 15.

see any effect Φ has to be increased to 0.5. In this case a minor effect is seen on the color of the spectrum and the peak-over-continuum strength of the 69 μm band. The strength of this band decreases because the continuum flux increases when more mass is ejected during the pre-superwind period.

Crystalline olivine distribution

In our standard model we only have crystalline olivine present in the superwind part of the outflow, but in this section we investigate if we can indeed rule out the presence of crystalline olivine in the low mass loss rate outflow preceding the superwind phase. Figure 18 shows the position and width of the 69 μm band when crystalline olivine is present in both the superwind and pre-superwind mass loss period for three superwind radii. From this we can directly see that the 69 μm band is dominated by the cold grains far away from the star since the feature is very narrow. The feature corresponds to grain temperatures between 100 and 150 K. Because the feature is dominated by the coldest crystalline olivine grains, the feature is not sensitive anymore to the superwind radius.

The presence of crystalline olivine in the old mass loss part of the outflow does not affect the strength of the 11.3 μm band (not shown). It does affect the peak-over-continuum strength of the 69 μm , which is large compared to the observations with values >0.08 (not shown).

Detectability of a previous superwind

In our standard model the star is currently in a superwind phase. If we assume that the superwind is linked to the thermal pulses of the star, then Vassiliadis & Wood (1993) show that for a 1 to 5 M_{\odot} star the period between thermal pulses is 50,000-100,000 years. For an outflow with a velocity of 10 km/s this roughly computes to a distance between two superwind phases of 100,000-200,000 AU. For our model we take a current superwind radius of 500 AU and a previous superwind at 100,000 AU with a radial size corresponding to 10,000 AU. Crystalline

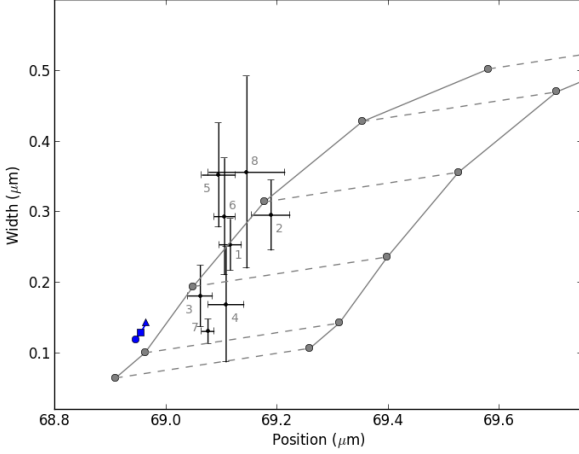


Fig. 18. The short blue curve connecting the circle, triangle and square in the lower left corner is for model 69 μm bands with a mass loss rate of $10 \cdot 10^{-5} \text{ M}_{\odot}/\text{yr}$. We also calculated model bands for the mass loss rates $1 \cdot 10^{-5} \text{ M}_{\odot}/\text{yr}$ and $5 \cdot 10^{-5} \text{ M}_{\odot}/\text{yr}$, but these are not distinguishable from the $10 \cdot 10^{-5} \text{ M}_{\odot}/\text{yr}$ models and they are not plotted. The circle, triangle and square are for superwind radii of 200, 500 and 2500 AU, respectively. In contrast to the standard model, in this case the crystalline olivine is also present in the pre-superwind mass loss period ejected before the superwind started. All other parameters are listed in table 3. For the rest, the figure is the same as fig. 14.

olivine is present in both these superwind phases but not in the low mass loss rate periods in-between.

Figure 19 shows that the peak-over-continuum strength of the 69 μm slightly increases when a second superwind is present. The width of the 69 μm band becomes slightly narrower, because the old superwind adds emission of cold crystalline olivine grains to the spectrum, but this effect is insignificant compared to the effect of the superwind radius on the width of the 69 μm band. The strength of the 11.3 μm band is not influenced by a previously ejected superwind wind, since this band is only sensitive to the dust close to the central star.

Metallic iron abundance

As a last parameter we also test the effect of the metallic iron abundance on the properties of the crystalline olivine bands. The outflow of the standard model contains 4% metallic iron and we now also test the cases where the outflow contains 8%, 1% or 0% iron. The results are shown in fig. 20. The metallic iron abundance does not have a significant effect on the strength of the 11.3 μm band. Metallic iron only has a minor effect on the color of the spectrum and the width and strength of the 69 μm band. It can be seen that less iron makes the spectrum redder, which is expected since metallic iron mostly adds opacity below $\sim 10 \mu\text{m}$.

Other parameters

Besides the parameters listed in this section we also tested the effects of the amorphous olivine composition and the outer radius of the total outflow. We tested the composition of amorphous olivine at the ratios $\left(\frac{\text{Amount}(\text{Mg}_2\text{SiO}_4)}{\text{Amount}(\text{MgFeSiO}_4)}\right)$ 0.2, 0.5 and 0.8. And we tested the outer radius at the values of 5,000 AU, 50,000 AU and 500,000 AU. It turned out that these two parameters have no ef-

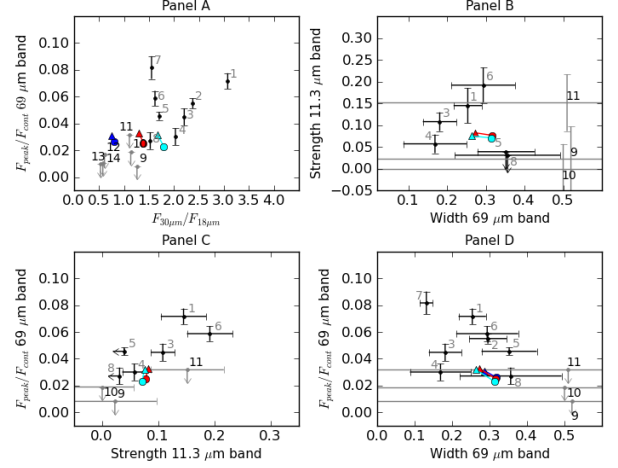


Fig. 19. The panels show different properties of model and observed spectra. The circle indicates a model with only one current superwind phase with a radius of 500 AU. The triangle indicates models that also have a **second superwind** at 100,000 AU of 10,000 AU long. The other properties are as in fig. 15.

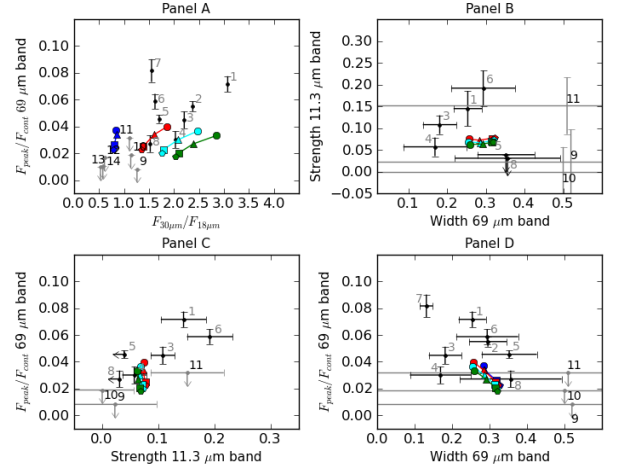


Fig. 20. The panels show different properties of model and observed spectra. The circle, triangle, square and pentagon markers indicate models with **metallic iron abundance** of 0%, 1%, 4% and 8%, respectively. The other properties are as in fig. 15

fect on the general shape of the spectrum or the properties of the spectral bands of crystalline olivine and the corresponding diagrams are not shown.

6. Results

The parameter study of the previous sections shows that:

- The width of the 69 μm band is only dependent on the superwind radius
- The strength of the 11.3 μm band is only dependent on the crystalline olivine abundance in the line of sight close to the star
- The peak-over-continuum strength of the 69 μm band is only dependent on the superwind radius and the crystalline olivine abundance

Panel B of fig. 21 shows the effect of the superwind radius and abundance on the width of the $69\ \mu\text{m}$ band and the strength of the $11.3\ \mu\text{m}$ band for the mass loss rate $15 \cdot 10^{-5}\ \text{M}_{\odot}/\text{yr}$. We can now use fig. 21B to read off the superwind radius and crystalline olivine abundance in the line of sight. We listed these values in table 4. The crystalline olivine abundance in the line of sight varies from lower than 2% to higher than 10%, which is comparable to that found by de Vries et al. (2010) using the same method. The superwind radii of the sources with $69\ \mu\text{m}$ bands can be as small as 200 AU and go up to ~ 2500 AU.

The abundance in the line of sight could not be determined for the sources with $9.7\ \mu\text{m}$ bands in-between an emission and absorption band (RAFGL 2374, WX Psc and IRC +50137). And for the sources with no detected $69\ \mu\text{m}$ bands (OH 104.91+2.4, AFGL 4259, IRAS 17010, RAFGL 2374, WX Psc and IRC +50137) we can only determine an upper limit of the size of the superwind radius. We argue that these six sources have no $69\ \mu\text{m}$ bands because they only contain very hot ($>300\ \text{K}$) crystalline olivine, since the opacities of such a population of hot crystalline olivine grains do not show a feature at $69\ \mu\text{m}$ even though they show a feature at $33.6\ \mu\text{m}$. In order to have an outflow with no cold and only hot crystalline olivine grains, we suggest that these sources have superwind radii smaller than 200 AU. Such a small superwind radius is also consistent with the fact that these sources have bluer infrared spectra compared to the other sources with larger superwind radii. Indeed Decin et al. (2007) showed that the current mass loss phase of WX Psc only extends up to ~ 50 AU.

Now that we know the superwind radii of our sources with $69\ \mu\text{m}$ bands, we can also derive a crystalline olivine abundance from the peak-over-continuum strength of the $69\ \mu\text{m}$ band. Panel D from fig. 21 shows the effect of the superwind radius and crystalline olivine abundance on the peak-over-continuum strength of the $69\ \mu\text{m}$ band. Table 4 lists the abundances derived from the $69\ \mu\text{m}$ band.

In the case the crystalline olivine abundance does not spatially vary in the outflow, both the abundance derived from the $11.3\ \mu\text{m}$ and the $69\ \mu\text{m}$ band must agree with each other. For the majority of the sources the abundance in the line of sight is indeed similar to that derived from the $69\ \mu\text{m}$ band, but a significant deviation is found for OH 127.8+0.0. For OH 127.8+0.0 the abundance in the line of sight is $<2\%$ while that derived from the $69\ \mu\text{m}$ band is $9 \pm 2\%$. That the abundance from the $11.3\ \mu\text{m}$ and the $69\ \mu\text{m}$ band agree for most of our sources, indicates that indeed the crystalline olivine is part of the outflow and not, for example, likely to be abundant in a stable disk-like structure embedded in the outflow.

The abundance mismatch found for OH 127.8+0.0 can either be due to a radial abundance gradient or a spherical abundance gradient in the outflow. A lower abundance from the $11.3\ \mu\text{m}$ band can be explained by having a lower abundance close to the star compared to farther away from the star. But since the superwind of OH 127.8+0.0 is only 400 ± 200 AU, this is not very plausible. It is more likely that the abundance of crystalline olivine is higher in the equatorial plane and that the equatorial plane is seen pole on. In that case the $69\ \mu\text{m}$ band would probe the full equatorial plane and result in a higher abundance than the $11.3\ \mu\text{m}$ band which only probes the line of sight towards the pole.

In the modeling section we also presented two scenarios where crystalline olivine is only present in the superwind or when it is also present in the mass loss period emitted before the superwind. When the crystalline olivine is also present in the pre-superwind mass loss period (with a mass loss rate of $>10\%$

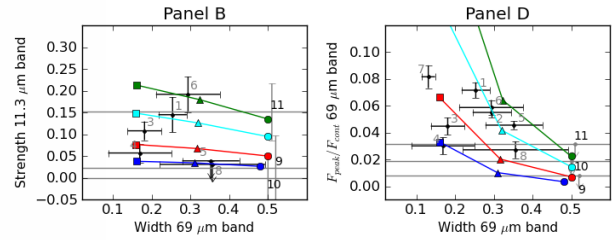


Fig. 21. The effect of the superwind radius and the crystalline olivine abundance on the 11.3 and $69\ \mu\text{m}$ band for models with a mass loss rate of $15 \cdot 10^{-5}\ \text{M}_{\odot}/\text{yr}$. The circle, triangle and square markers indicate models with **superwind radii** of 200, 500 and 2500 AU respectively. The blue, red, teal and green curves now represent the **crystalline olivine abundances** of 2, 4, 8 and 12 %. The other parameters of the models are as in the standard mode. The other properties are as in fig. 15.

that of the superwind phase) the $69\ \mu\text{m}$ bands are so narrow and so strong that they do not compare well with our observed sources (see fig. 18). This shows that the crystalline olivine is only present in the superwind part of the outflow.

We also tested the presence of a previously emitted superwind containing crystalline olivine. From fig. 19 it can be seen that the effect of a previously emitted superwind on the $11.3\ \mu\text{m}$ and $69\ \mu\text{m}$ band is small and that we can therefore not rule out the presence of such a previously emitted superwind.

The composition of the crystalline olivine in the outflow of these OH/IR stars is discussed by Blommaert et al. (in prep.). They show, using fig. 11, that the crystalline olivine contains almost no iron (0-0.5%). If we compare the width and position of the $69\ \mu\text{m}$ bands with the models with different superwind radii in fig. 14, we might see a slight difference in iron content as a function of superwind radius. The OH/IR stars with the smallest superwind radii (for example AFGL 5379 and OH 127.8+0.0) correspond very well with our models using pure forsterite (no iron). On the other hand, the sources with larger superwind radii (for example IRAS 21554 and OH 26.5+0.6) have slightly red shifted $69\ \mu\text{m}$ bands and the crystalline olivine might contain a small amount of iron ($<0.5\%$).

7. Discussion and Conclusions

Since the crystalline olivine is part of the superwind, we can take the crystalline olivine as a tracer of the bulk of the dust in the superwind. This means that the width of the $69\ \mu\text{m}$ bands shown in fig. 14 can only be explained if the superwind radii of these stars is smaller than $\sim 2500\ \text{AU} = 1400\ R_{*}$. A maximum superwind radius of 2500 AU means, assuming an outflow velocity of 10-15 km/s, that the outflow started roughly $\lesssim 1200$ -800 years ago.

Recently more evidence has been found that indeed the duration of the superwind is very short. The study, based on SED modeling and OH and CO observations, of Justtanont et al. (2006) showed for several stars (among others OH 30.1-0.7, OH 26.5+0.6, OH 21.5+0.5, OH 32.8-0.3 and AFGL 5379) that the superwind must have started <2000 years ago.

Based on CO observations Justtanont et al. (2013) find superwind durations shorter than 300 years, for five objects that are also in our sample (WX Psc, OH 127.8+0.0, AFGL 5379, OH 26.5+0.6 and OH 30.1-0.7). The <300 years found by Justtanont et al. (2013) corresponds to a superwind radius of

Source name	#	11.3 μm	69 μm	R_{SW} (AU)	$A_{11.3}$ (%)	A_{69} (%)
OH 32.8-0.3	1	+	+	1,500 \pm 400	8 \pm 2	7 \pm 2
OH 21.5+0.5	2	?	+	1,250 \pm 250	?	7 \pm 2
OH 30.1-0.7	3	+	+	2,500 \pm 300	5 \pm 2	3 \pm 1
OH 26.5+0.6	4	+	+	2,500 \pm 1,000	3 \pm 1	2 \pm 1
OH 127.8+0.0	5	-	+	400 \pm 200	<2	9 \pm 2
AFGL 2403	6	+	+	700 \pm 400	11 \pm 3	8 \pm 2
IRAS 21554	7	?	+	2,800 \pm 300	?	4 \pm 2
AFGL 5379	8	-	+	400 $^{+1000}_{-200}$	<2	5 \pm 3
OH 104.91+2.4	9	-	-	<200	<2	<2
AFGL 4259	10	-	-	<200	<2	<2
IRAS 17010	11	+	-	<200	10 \pm 4	<12
RAFGL 2374	12	?	-	<200	?	.
WX Psc	13	?	-	<200	?	.
IRC +50137	14	?	-	<200	?	.

Table 4. List of the observed OH/IR stars and modeling results. The two columns 11.3 μm and 69 μm list if these bands of crystalline olivine are detected. The next columns lists the superwind radii found from the 69 μm band, the crystalline olivine abundance derived from the 11.3 and that derived from the 69 μm band.

<600 AU. In the case of WX Psc, OH 127.8+0.0 and AFGL 5379 this corresponds well with our findings (see table 4), but the superwind radius we find for OH 26.5+0.6 and OH 30.1-0.7 is larger than that of Justtanont et al. (2013). Independent SED modeling of OH 26.5+0.6 (Groenewegen 2012; Chesneau et al. 2005) resulted in a superwind radius for this object of \sim 500 AU, which is smaller than the 2500 \pm 1000 AU that we find.

The mass loss rates of OH/IR stars can go up to $15 \cdot 10^{-5} M_{\odot}/\text{yr}$ and even slightly higher (Justtanont et al. 1996; Justtanont & Tielens 1992; Schutte & Tielens 1989; Groenewegen 1994). If we combine these mass loss rates with the timescales we derive, we find a total mass in the superwind of \sim 0.2 M_{\odot} (at a gas over dust ratio of 100). The gas over dust ratio can be as high as 200-300 (Lombaert et al. 2013), meaning the star could lose 0.2-0.6 M_{\odot} in one superwind phase. Depending on the initial mass of the star, one superwind could already contain enough mass for the AGB star to evolve away from the AGB.

One object that is known to originate from an OH/IR star and that just ascended the post-AGB is HD 161796. This object has been extensively analyzed by Hoogzaad et al. (2002) and Min et al. (2013) and is shown to have stopped its mass loss only \sim 300 years ago. HD 161796 now has an expanding oxygen-rich dust shell that contains \sim 0.05 M_{\odot} of gas and dust (Min et al. 2013 and private communication). This mass is consistent with the mass we find that an OH/IR stars can lose in one superwind phase. The mass of HD 161796 before it ascended the AGB is found to be \sim 1 M_{\odot} (Kipper 2007; Stasińska et al. 2006), making this object an example of a star with a low mass that left its AGB phase with only one superwind phase. In the case of OH/IR stars with higher progenitor masses, the star would need to go through several superwind phases before it could leave the AGB phase.

There are strong indications that the OH/IR stars in our sample have high initial masses ($\geq 5 M_{\odot}$). First of all most of our objects have long periods (order of \sim 1000 days) and/or high luminosities ($>10,000 L_{\odot}$) and they are situated at low galactic latitudes (van Langevelde et al. 1990 and De Beck et al. 2010 and references therein, see table 1). Furthermore, based on the $^{12}\text{C}/^{13}\text{C}$ and $^{18}\text{O}/^{17}\text{O}$ ratio it is shown that most of our sources have experienced hot-bottom burning (Delfosse et al. 1997; Justtanont et al. 2013), indicating that they must have a high initial mass ($\geq 5 M_{\odot}$). OH/IR stars with such high progenitor masses need to lose several solar masses before they can leave the AGB.

Therefore we expect to see several superwind phases as extended shells around the OH/IR stars in our sample, in the same way as these extended shells are seen around carbon-rich AGB stars (Cox et al. 2012; Maercker et al. 2012).

Using the methods in this paper we can not study any previously emitted superwinds because the width and strength of the 69 μm band are not sensitive to the presence of previously emitted superwind phases. But it is intriguing that even though several oxygen-rich AGB stars have been observed with Herschel, none of them show any extended structure (Cox et al. 2012). If this is an indication of the fact that these OH/IR stars indeed have no extended shells and thus no previously emitted superwinds, then it is hard to understand how these OH/IR stars lose enough mass to evolve away from the AGB.

The next step in understanding the evolution of these OH/IR stars is to systematically search for extended material around these stars. This would show if these objects have gone through one or several superwind phases. If it is indeed the case that OH/IR stars only have one superwind, then these stars need to lose their mass in another way. We hypothesize that these OH/IR stars evolve into an as of yet unrecognized type of object with an even more extremely high and abrupt mass loss phase. Such an object would have an SED so extremely red it would not necessarily be recognized as an OH/IR star.

The post-AGB or proto-PN IRAS 16342–3814 could be an example of such an object, since its SED is extremely red. The SED shows no flux at wavelengths at and below 10 μm and peaks around \sim 40 μm (Dijkstra et al. 2003). The crystalline olivine bands seen in the spectrum of IRAS 16342–3814 are also in absorption up to 45 μm . The object has an almost spherical dust shell that is punctured by bipolar jets (Verhoelst et al. 2009). The mass loss rate it must have had on the AGB is of the order of $10^{-3} M_{\odot}/\text{yr}$ (Verhoelst et al. 2009). Maybe OH/IR stars with massive progenitors evolve into a phase like that of IRAS 16342–3814, in which they develop an even higher mass loss rate for a short duration after which they directly evolve away from the AGB.

Acknowledgements. B.L. de Vries acknowledges support from the Fund for Scientific Research of Flanders (FWO) for his Aspirant fellowship as well as under grant number G.0470.07.

References

- Bedijn, P. J. 1987, A&A, 186, 136
- Bohren, C. F. & Huffman, D. R. 1983, Absorption and scattering of light by small particles (New York: Wiley, 1983)
- Bowen, G. H. 1988, ApJ, 329, 299
- Castor, J. I. 1981, in *Astrophysics and Space Science Library*, Vol. 88, Physical Processes in Red Giants, ed. I. Iben, Jr. & A. Renzini, 285–299
- Chesneau, O., Verhoelst, T., Lopez, B., et al. 2005, A&A, 435, 563
- Cox, N. L. J., Kerschbaum, F., van Marle, A.-J., et al. 2012, A&A, 537, A35
- De Beck, E., Decin, L., de Koter, A., et al. 2010, A&A, 523, A18
- de Vries, B. L., Acke, B., Blommaert, J. A. D. L., et al. 2012, *Nature*, 490, 74
- de Vries, B. L., Min, M., Waters, L. B. F. M., Blommaert, J. A. D. L., & Kemper, F. 2010, A&A, 516, A86
- Decin, L. 2012, *Advances in Space Research*, 50, 843
- Decin, L., Hony, S., de Koter, A., et al. 2007, A&A, 475, 233
- Delfosse, X., Kahane, C., & Forveille, T. 1997, A&A, 320, 249
- Dijkstra, C., Waters, L. B. F. M., Kemper, F., et al. 2003, A&A, 399, 1037
- Gail, H.-P. & Sedlmayr, E. 1999, A&A, 347, 594
- Groenewegen, M. A. T. 1994, A&A, 290, 544
- Groenewegen, M. A. T. 2012, A&A, 543, A36
- Groenewegen, M. A. T., Waelkens, C., Barlow, M. J., et al. 2011, A&A, 526, A162
- Habing, H. J. & Olofsson, H., eds. 2003, *Asymptotic giant branch stars*
- Hearn, A. G. 1990, in *From Miras to Planetary Nebulae: Which Path for Stellar Evolution?*, ed. M. O. Mennessier & A. Omont, 121–130
- Heske, A., Forveille, T., Omont, A., van der Veen, W. E. C. J., & Habing, H. J. 1990, A&A, 239, 173
- Holzer, T. E. & MacGregor, K. B. 1985, in *Astrophysics and Space Science Library*, Vol. 117, Mass Loss from Red Giants, ed. M. Morris & B. Zuckerman, 229–255
- Hoogzaad, S. N., Molster, F. J., Dominik, C., et al. 2002, A&A, 389, 547
- Iben, Jr., I. & Renzini, A., eds. 1981, *Astrophysics and Space Science Library*, Vol. 88, Physical processes in red giants; Proceedings of the Second Workshop, Advanced School of Astronomy, Erice, Italy, September 3–13, 1980
- Jäger, C., Molster, F. J., Dorschner, J., et al. 1998, A&A, 339, 904
- Jones, O. C., Kemper, F., Sargent, B. A., et al. 2012, ArXiv e-prints
- Justtanont, K., Olofsson, G., Dijkstra, C., & Meyer, A. W. 2006, A&A, 450, 1051
- Justtanont, K., Skinner, C. J., Tielens, A. G. G. M., Meixner, M., & Baas, F. 1996, ApJ, 456, 337
- Justtanont, K., Teyssier, D., Barlow, M. J., et al. 2013, ArXiv e-prints
- Justtanont, K. & Tielens, A. G. G. M. 1992, ApJ, 389, 400
- Kemper, F., de Koter, A., Waters, L. B. F. M., Bouwman, J., & Tielens, A. G. G. M. 2002, A&A, 384, 585
- Kemper, F., Waters, L. B. F. M., de Koter, A., & Tielens, A. G. G. M. 2001, A&A, 369, 132
- Kipper, T. 2007, *Baltic Astronomy*, 16, 191
- Knapp, G. R. & Morris, M. 1985, ApJ, 292, 640
- Koike, C., Chihara, H., Tsuchiyama, A., et al. 2003, A&A, 399, 1101
- Li, A. & Draine, B. T. 2001, ApJ, 550, L213
- Lombaert, R., Decin, L., de Koter, A., et al. 2013, A&A, 554, A142
- Maercker, M., Mohamed, S., Vlemmings, W. H. T., et al. 2012, *Nature*, 490, 232
- Min, M., Dullemond, C. P., Dominik, C., de Koter, A., & Hovenier, J. W. 2009, A&A, 497, 155
- Min, M., Jeffers, S. V., Canovas, H., et al. 2013, ArXiv e-prints
- Norris, B. R. M., Tuthill, P. G., Ireland, M. J., et al. 2012, *Nature*, 484, 220
- Ordal, M. A., Bell, R. J., Alexander, Jr., R. W., Newquist, L. A., & Querry, M. R. 1988, *Appl. Opt.*, 27, 1203
- Ott, S. 2010, in *Astronomical Society of the Pacific Conference Series*, Vol. 434, Astronomical Data Analysis Software and Systems XIX, ed. Y. Mizumoto, K.-I. Morita, & M. Ohishi, 139
- Pilbratt, G. L., Riedinger, J. R., Passvogel, T., et al. 2010, A&A, 518, L1
- Poglitsch, A., Waelkens, C., Geis, N., et al. 2010, A&A, 518, L2
- Riechers, D., Balega, Y., Driebe, T., et al. 2005, A&A, 436, 925
- Schutte, W. A. & Tielens, A. G. G. M. 1989, ApJ, 343, 369
- Sloan, G. C., Kraemer, K. E., Price, S. D., & Shipman, R. F. 2003, ApJS, 147, 379
- Sogawa, H. & Kozasa, T. 1999, ApJ, 516, L33
- Speck, A. K., Whittington, A. G., & Tartar, J. B. 2008, ApJ, 687, L91
- Stasińska, G., Szczerba, R., Schmidt, M., & Siódmiak, N. 2006, A&A, 450, 701
- Sturm, B., Bouwman, J., Henning, T., et al. 2013, ArXiv e-prints
- Suto, H., Sogawa, H., Tachibana, S., et al. 2006, MNRAS, 370, 1599
- Tielens, A. G. G. M., Waters, L. B. F. M., Molster, F. J., & Justtanont, K. 1998, Ap&SS, 255, 415
- van Langevelde, H. J., van der Heiden, R., & van Schooneveld, C. 1990, A&A, 239, 193
- Vassiliadis, E. & Wood, P. R. 1993, ApJ, 413, 641
- Verhoelst, T., Waters, L. B. F. M., Verhoeff, A., et al. 2009, A&A, 503, 837
- Waters, L. B. F. M., Molster, F. J., de Jong, T., et al. 1996, A&A, 315, L361
- Wood, P. R. 1979, ApJ, 227, 220
- Wood, P. R., Whiteoak, J. B., Hughes, S. M. G., et al. 1992, ApJ, 397, 552